Dominant Anomaly Patterns in the Near-Surface Baroclinicity and Accompanying Anomalies in the Atmosphere and Oceans. Part II: North Pacific Basin

MOTOTAKA NAKAMURA* AND SHOZO YAMANE†

Japan Agency for Marine-Earth Science and Technology, Yokohama, Kanagawa, Japan

ABSTRACT

Variability in the monthly-mean flow and storm track in the North Pacific basin is examined with a focus on the near-surface baroclinicity. Dominant patterns of anomalous near-surface baroclinicity found from EOF analyses generally show mixed patterns of shift and changes in the strength of near-surface baroclinicity. Composited anomalies in the monthly-mean wind at various pressure levels based on the signals in the EOFs show accompanying anomalies in the mean flow up to 50 hPa in the winter and up to 100 hPa in other seasons. Anomalous eddy fields accompanying the anomalous near-surface baroclinicity patterns exhibit, broadly speaking, structures anticipated from simple linear theories of baroclinic instability, and suggest a tendency for anomalous wave fluxes to accelerate–decelerate the surface westerly accordingly. However, the relationship between anomalous eddy fields and anomalous near-surface baroclinicity in the midwinter is not consistent with the simple linear baroclinic instability theories. Composited anomalous SST accompanying anomalous near-surface baroclinicity often exhibits moderate values and large spatial scales in the basin, rather than large values concentrated near the oceanic fronts. In the midsummer and in some cases in cold months, however, large SST anomalies are found around the Kuroshio–Oyashio Extensions. Accompanying anomalies in the net surface heat flux, SST in the preceding and following months, and meridional eddy heat flux in the lower troposphere suggest active roles played by the ocean in generating the concomitant anomalous large-scale atmospheric state in some of these cases.

1. Introduction

It has now become our basic knowledge that the extratropical atmosphere is driven strongly by the horizontal potential temperature gradient that arises from the differential solar heating (e.g., Lorenz 1955). The horizontal gradient in the potential temperature, often referred to as baroclinicity, is a measure of upper-level wind steering via thermal wind and a measure of baroclinic instability in the atmosphere. Baroclinicity in the lower atmosphere in classic theories of atmospheric stability is measured by a combination of the static stability and horizontal temperature gradient, the latter of which is equivalent to vertical shear in the horizontal wind through the thermal wind balance (Charney 1947; Eady 1949). In its original form, the Eady's maximum growth rate for baroclinic instability B_{GRMax} is defined by $B_{GRMax} = 0.31(|f|/N)(\partial U/\partial z)$ in a zonally homogeneous steady mean state, where U is the mean zonal flow, f is the Coriolis parameter, and N is the

Brunt–Väisälä frequency. Charney's formula is slightly different from the Eady's, but still incorporates the same effects.

Lindzen and Farrell (1980) first applied the Eady's parameter to atmospheric data to successfully estimate the maximum growth rate of baroclinic instability in the troposphere. Hoskins and Valdes (1990) used its localized version (i.e., U, N, and f are all local Eulerian mean values) as the central parameter in their study of the Northern Hemispheric storm tracks. This local version, or its simplified version, has been used successfully as an indicator of baroclinic wave generation in diagnostic studies of stormtracks in recent years as well (Nakamura and Sampe 2002; Nakamura and Shimpo 2004; Nakamura et al. 2004). In our study, the North Atlantic part of which was reported in Nakamura and Yamane (2009, hereafter Part I), we define the near-surface baroclinic vector, $\mathbf{B} = B^x\mathbf{i} + B^y\mathbf{j}$, where $B^x = -(g/\theta N)(\partial\theta/\partial y)$ and $B^y = (g/\theta N)(\partial\theta/\partial x)$ with θ being the monthly-mean potential temperature at 2 m above the surface, and use it as the central quantity of the diagnoses. Unless stated otherwise, "anomalies" refer to deviations from the climatology hereafter. Though its meridional component does not appear in any classic theory of baroclinic instability, a theory that does incorporate the effect of B^y shows its important

Corresponding author address: Mototaka Nakamura, Japan Agency for Marine-Earth Science and Technology, 3173-25 Showamachi, Kanazawa-ku, Yokohama, Kanagawa 236-0001, Japan.
E-mail: moto@jamstec.go.jp

†Current affiliation: Science and Engineering, Doshisha University, Kyotanabe, Kyoto, Japan.

role in enhancing baroclinic wave generation locally to the east of the mean trough (Niehaus 1980). In the North Atlantic storm track region, we indeed found that the substantial zonal gradient in the surface temperature in and around the Labrador Sea plays a major role in the large-scale atmospheric state.

2. The sea surface temperature

The sea surface temperature (SST) is an important factor in determining $\mathbf{B}$ in the storm-track regions (e.g., Hoskins and Valdes 1990; Nakamura et al. 2004; Part I). SST anomalies (SSTAs) around an oceanic front along the Gulf Stream (GS), Kuroshio Extension (KE), or Oyashio Extension (OE) can have a profound impact on $\mathbf{B}$ along the storm tracks.

a. A subtle point

A subtle but important point that has to be considered carefully in this regard is the spatial scale and the location of SSTAs with respect to the climatology, since it is the anomalous surface temperature gradient whose structure has a spatial scale of the atmospheric Rossby deformation radius that can exert significant influence on the large-scale atmospheric flow.

1) CHANGES IN THE TEMPERATURE

The high sensitivity of $\mathbf{B}$ to changes in the temperature contrast across the front and changes in the width of the front, and the uncertainty in the impact of SSTAs of small spatial scales on $\mathbf{B}$ make it difficult to assess the effective B anomalies that are attributable to the SSTAs from the available data. Moreover, it is uncertain exactly how the SSTAs in the presence or absence of the land surface temperature anomalies may or may not produce $\mathbf{B}$ anomalies that are significant to the atmosphere.

(i) Complicating factor The complicating factor introduced by the land surface must be taken into account when studying potential roles of extratropical SSTAs in the extratropical atmospheric anomalies.

Lau (1988) investigated patterns of anomalous storm track activity and associated low-frequency flow anomalies by computing empirical orthogonal functions (EOFs) for high-frequency 500-hPa geopotential height for the Northern Hemisphere winters. He found that both North Atlantic and North Pacific storm tracks have a pattern of meridional shift and a pattern of increased or decreased eddy activity in the first two EOFs. He also found that these changes in the storm tracks have symbiotic relationships with the background flows and have substantial impacts on the mean flow. Part I approached the issue of the storm track and low-frequency flow variability in connection with SSTAs in the extratropics, focusing on $\mathbf{B}$ as the key parameter of diagnoses, and found similar patterns of

TABLE 1. Percentage of variance explained by the first four EOFs for the North Pacific Bx. The degree of separation between EOF1 and EOF2 and EOF2 and EOF3, based on the North et al. (1982) criterion, is indicated by good (GD) and not good or marginal (NG).

Month	EOF1	Split	EOF2	Split	EOF3	EOF4
Jan	29	NG	24	GD	10	5
Feb	39	GD	20	GD	7	6
Mar	31	GD	14	NG	10	6
Apr	23	GD	14	NG	10	7
May	19	GD	12	NG	10	7
Jun	19	GD	12	NG	10	9
Jul	18	NG	13	NG	9	7
Aug	18	NG	13	NG	11	9
Sep	17	NG	13	NG	10	8
Oct	16	NG	13	GD	8	7
Nov	19	NG	16	NG	11	8
Dec	33	GD	18	GD	10	6

variability in the eddy activity and low-frequency flow in the North Atlantic basin. Much of this variability was connected to SSTAs in the vicinity of the Gulf Stream in cold months (Part I). Since the winter North Pacific basin has a storm track and mean flow that appear to be related to the oceanic fronts, Kuroshio–Oyashio Extensions (KOE) in this case, in a manner essentially the same as those in the North Atlantic basin related to the GS, we have attempted to find similar results for the North Pacific basin. In this regard, we have chosen not to project our results onto the major mode of variability in the extratropical North Pacific basin, the North Pacific decadal variability (PDV), so that our presentation and discussion are mostly confined to the wave–mean flow dynamics of monthly time scale or shorter.

Our approach to the search for a link between anomalies in the KOE and the overlying atmosphere is as follows: (i) identify dominant patterns in anomalous $\mathbf{B}$ in the storm track for each calendar month and identify years in which the anomaly fits the pattern well, (ii) composite anomalies in the monthly-mean circulation and high frequency transients in the atmosphere to obtain a typical atmospheric state that accompanies the patterns of anomalous $\mathbf{B}$, (iii) composite SSTA to obtain a typical oceanic state that accompanies and precedes the patterns of anomalous $\mathbf{B}$, and (iv) composite anomalous net surface heat flux that accompanies and precedes the pattern of anomalous $\mathbf{B}$. With this approach, we obtain typical pictures of anomalous states in the atmosphere and oceans with anomalous $\mathbf{B}$ as their connecting interface. Section 2 describes the data and procedure to compute $\mathbf{B}$. Section 3 describes the climatology and variance of $\mathbf{B}$. Dominant patterns of $\mathbf{B}$ are shown in section 4, followed by composited anomalies in various atmospheric fields and SST in section 5. Finally, we present our discussion on the results, examining a potential cause–
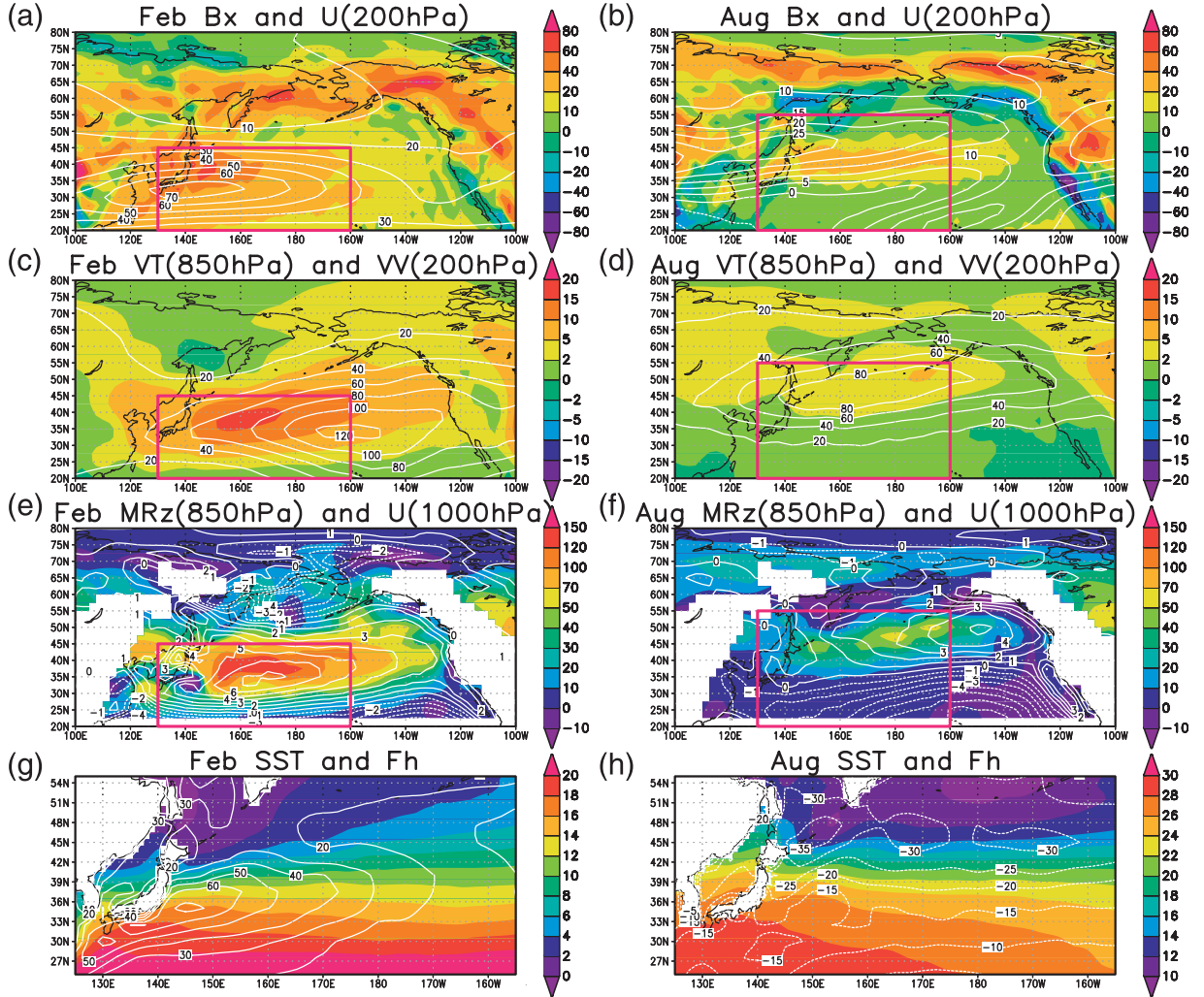
FIG. 1. Climatology of $Bx(10^{-6}s^{-1}$, color) and U^{200}(m s^{-1}, contours) for (a) February and (b) August; $\overline{V'\theta'}^{850}$ (K m s^{-1}, color) and $\overline{V'V'}^{200}$ (m^2 s^{-1}, contours) for (c) February and (d) August; MR^{z850} (10^{-3} m^2 s-2, color) and U^{1000} (m s^{-1}, contours) for (e) February and (f) August; and SST (K, color) and F_h [10^5 J m^{-2} (6 h)$^{-1}$] for (g) February and (h) August. Red rectangles indicate the domain of EOF calculations.

effect relationship between anomalies in the SST and atmosphere in section 6.

Figure 1 shows the climatology of Bx, U^{200}, $\overline{V'\theta'}^{850}$, $\overline{V'\theta'}^{200}$, MR^{z850}, U^{1000}, SST, and F_h for February and August as examples of the reference state in the winter and summer. The numeric superscript indicates the pressure level in hPa. The seasonal mean is visibly more diffused in structure, particularly for Bx, than those shown in Fig. 1. There are no surprises in the overall picture of Bx. The regions of large land–sea temperature contrast and the oceanic fronts show very large Bx in cold months. The position of Bx maximum in the storm track region is found along the KOE region throughout the year. The zonally elongated band of large Bx in the storm track is generally wider in cold months than in warm months. In fact,

large Bx values that presumably accompany the Kuroshio and its extension in the cold months vanish in the summer (Figs. 1a,b). The seasonal variation in the Bx values in the storm track basically follows that of the north–south differential heating–largest in the winter and smallest in the summer. As reported by Nakamura et al. (2004), the U^{200} maximum is displaced southward from the Bx maximum visibly in winter months (Fig. 1a), although U200 is generally large over the area of large Bx in the core of the storm track. The southward displacement of the U200 maximum from the Bx maximum in the storm track is less pronounced or even reversed in warmer months (Fig. 1b). We note that the structure of the climatological Bx generally reflects those of $(\partial\theta^{2m}/\partial y)$ with some exceptions where the surface slope contributes significantly to Bx in

TABLE 2. Years selected for anomaly composites for the positive phase of B^x EOF1.

Month	Yr of positive phase
Jan	1961, 1969, 1978, 1979, 1988, 1990, 1992, 1994
Feb	1964, 1977, 1978, 1980, 1983, 1986, 1988, 2000, 2001
Mar	1970, 1973, 1979, 1980, 1984, 1988, 2000
Apr	1959, 1961, 1962, 1963, 1968, 1972, 1983, 2002
May	1971, 1984, 1993, 1996, 2000
Jun	1981, 1983, 1984, 1993, 1998
Jul	1961, 1972, 1973, 1978, 1994, 2000
Aug	1967, 1970, 1973, 1978, 1994, 1999
Sep	1975, 1977, 1988, 1989, 1994, 1998, 1999
Oct	1962, 1977, 1998, 1999, 2001
Nov	1985, 1986, 1987, 1988, 1991, 1998
Dec	1957, 1968, 1972, 1978, 1979, 1990

TABLE 3. Years selected for anomaly composites for the negative phase of B^x EOF1.

Month	Yr of negative phase
Jan	1962, 1963, 1968, 1974, 1991, 1996, 1997
Feb	1959, 1963, 1971, 1974, 1976, 1979, 1985, 1989, 1990, 1994
Mar	1963, 1968, 1972
Apr	1984, 1988, 1993, 1996, 1999, 2000
May	1961, 1963, 1983, 1987, 1997
Jun	1961, 1972, 1978, 1980, 1982, 1986
Jul	1964, 1974, 1980, 1983, 1986, 1988, 1993
Aug	1980, 1987, 1991, 1993, 1997
Sep	1959, 1963, 1969, 1983, 1985, 1993
Oct	1957, 1986, 1993, 1996, 1997
Nov	1958, 1968, 1970, 1982, 1997
Dec	1969, 1974, 1976, 1985, 1998, 1999, 2000, 2001

isolated areas over the land, most notably around the Himalayas.

The position and structure of the storm track as indicated by $\overline{V'\theta'}^{850}$ and $\overline{V'V'}^{200}$ are, at least for the winter, essentially the same as those reported in earlier studies on the storm tracks (e.g., Chang et al. 2002). The maxima in $\overline{V'\theta'}^{850}$ and $\overline{V'V'}^{200}$ are located in the band of large Bx.

3. Data and calculation procedures

The data used to calculate **B** are the monthly-mean temperature at 2 m above the surface (T^{2m}) and temperature at pressure levels available from the 40-yr European Centre for Medium-Range Weather Forecasts (ECMWF) Re-Analysis (ERA-40; Uppala et al. 2005). We chose the ERA-40 T^{2m} data rather than the National Centers for Environmental Prediction–National Center for Atmospheric Research (NCEP–NCAR) reanalysis products for its explicit inclusion of the observed near-surface temperature in producing the T^{2m} data. The monthly-mean surface pressure data from the NCEP–NCAR reanalyses (Kalnay et al. 1996) were used to determine the pressure levels to

be used for **B** calculation, and to calculate θ at 2 m above the surface from T^{2m}. We used the NCEP–NCAR surface pressure data for convenience, since we had already compiled the dataset for calculating transient eddy fluxes to be mentioned later and the ERA-40 surface pressure data are not readily available. We later compared the NCEP–NCAR monthly-mean sea level pressure with that of ERA-40, and found the difference between the two products to be immaterial for the purpose of the current study. We also used ERA-40 monthly-mean horizontal wind and geopotential height at pressure levels, net surface heat flux, Fh (the sum of latent heat flux, sensible heat flux, solar radiation, and the thermal radiation), and Hadley Centre sea surface temperature data (Rayner et al. 2003) to compile anomaly composites accompanying anomalous patterns in **B**. In addition, we used 6-hourly temperature and wind data from the NCEP–NCAR reanalyses to compute various eddy fields. The accuracy of the Fh data used here is, as true for other reanalyses surface heat flux products, may not be so high to produce reliable anomaly composites.

We computed **B** near the surface by calculating the horizontal gradient in θ^{2m}, using the centered finite differencing, and calculating N from the lowest three vertical pressure levels that are location dependent because of topography. Both $\nabla\theta^{2m}$ and N were calculated locally as in Hoskins and Valdes (1990) and Nakamura and Shimpo (2004). The entire 45 yr from September 1957 to August 2002 were used for the Northern Hemisphere. To resolve the dominant modes in **B** arising from the land–sea temperature contrast, one may need much higher horizontal resolution in the data. The relatively coarse horizontal resolution of the data may artificially suppress the significance of the variability associated with the land–sea temperature contrast.One should keep this limitation in mind. The 6-hourly bandpassed (period of 2–7 days) eddy fields and ultra-low-frequency (period of 30 days and longer) background fields were computed from the NCEP–NCAR reanalyses, using simple time filters (Lau and Lau 1984) first. The filtered time series were then visually examined against the raw time series and, then, used to calculate the slowly evolving bandpassed meridional velocity variance ($\overline{V'V'}$), meridional temperature flux ($\overline{V'\theta'}$), and the three-dimensional transient wave activity flux defined on a zonally varying basic state by Plumb (1986). The wave activity flux consists of the zonal and meridional advective fluxes (MU and MV), the zonal and meridional radiative fluxes (MRx and MRy), and the radiative vertical flux (MRz). The flux is essentially the Eliassen–Palm flux (Eliassen and Palm 1961) in a zonally inhomogeneous mean flow (Plumb 1986). The wave activity flux was calculated from February 1948 to November 2004 only for the extratropics poleward of 208 latitude. Also, it was calculated only from 850 to 30 hPa because of the double differentiation with respect to pressure required for the calculation. The flux of particular interest in this study is
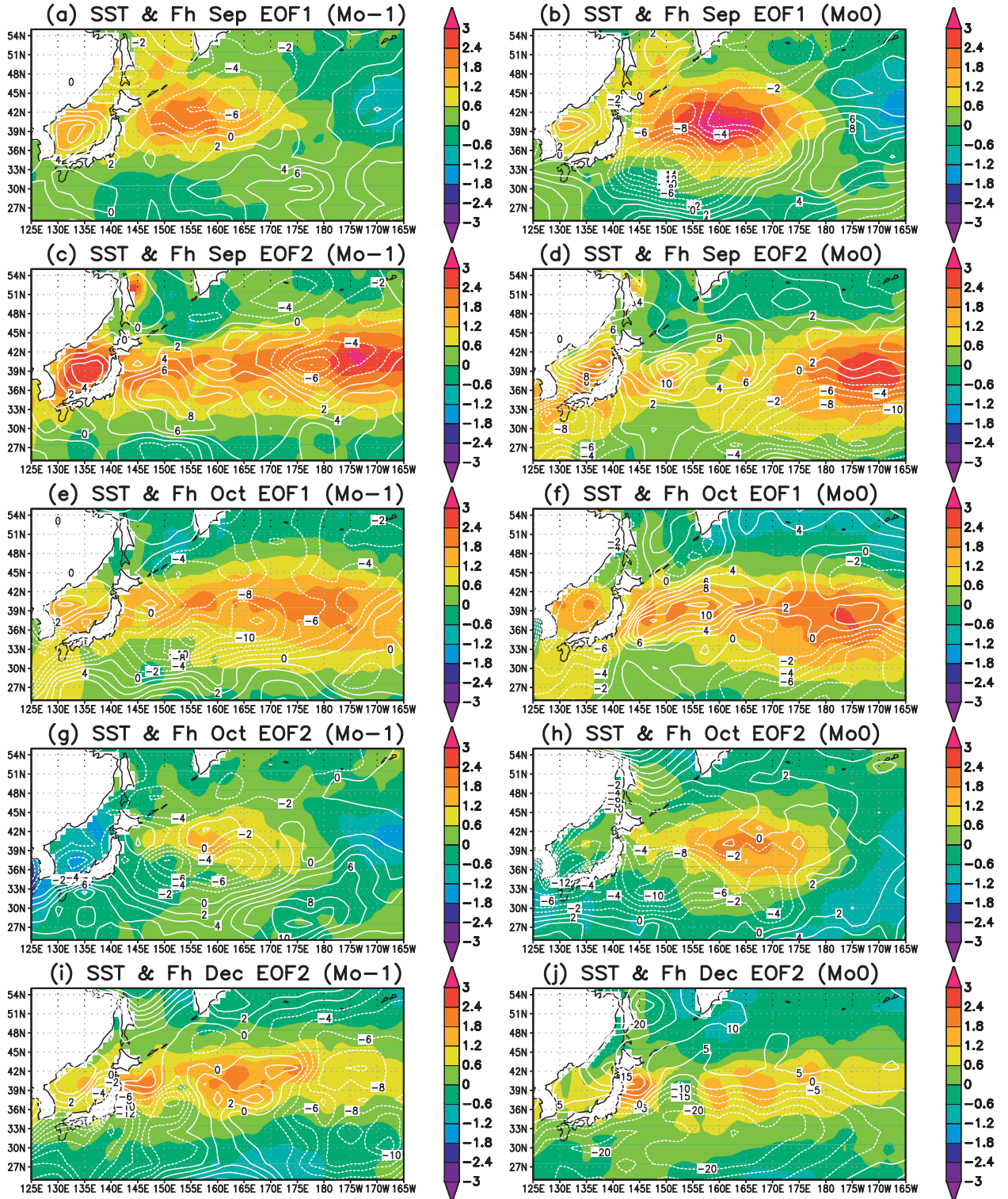
FIG. 2. As in Fig. 10, but for (a),(b) September EOF1; (c),(d) September EOF2; (e),(f) October EOF1; (g),(h) October EOF2; and (i),(j) December EOF2.

the vertical component. Here MR^z is defined by

$$MR^z = \frac{pf\cos\phi}{p^0|\nabla h\bar{q}|(d\theta_0/dz)}\left(\frac{\partial\bar{q}}{\partial x}\overline{U'\theta'} + \frac{\partial\bar{q}}{\partial y}\overline{V'\theta'}\right),$$

where q is quasigeostrophic potential vorticity, p is the pressure, p^0 is the reference surface pressure set to 1000 hPa here, θ_0 is the area-weighted ultra-low-frequency hemispheric mean potential temperature at each height, u9 is the bandpassed potential temperature, and z is the geopotential height. An overbar denotes an ultra-low frequency component and a prime denotes bandpassed component. The 6-hourly time series of wave fluxes was computed by using the time series of ultra-low-frequency fields as the basic-state and high-frequency fields as eddies. In short, the time series was calculated by changing the meaning of an overbar from the time mean state to an ultra-low-frequency state, and changing the meaning of a prime from a departure from the mean to a high-frequency state. The 6-hourly eddy time series was averaged over each month to produce monthly-mean time series. This dataset allows us to examine anomalous eddy fields accompanying anomalous **B** in specific months. The climatology for the eddy fields was computed from 46 yr, January 1958 to December 2003. The calculation of the wave activity and its flux is described in detail by Nakamura et al. (2010).

4. Climatology and variance

The climatology and variance of *Bx* and *By* were computed for each calendar month and examined closely for their spatial and temporal structures. The monthly climatology, rather than the seasonal climatology, is used as the reference in our study, to avoid contamination of the diagnostic results arising from differences in the climatology between two successive months. Unlike in the North Atlantic basin reported in Part I, we found the impact of *By* variations on the large-scale atmospheric state in the North Pacific basin much weaker than that of Bx variations, presumably because of themore zonal orientation of the KOE in comparison to the Gulf Stream and North Atlantic Current. In the following, thus, we focus our presentation on the climatology and variations of *Bx* and their impact on the large-scale atmospheric state.

Sample citations: Becker and Schmitz (2003), Knutti et al. (2008), and (Meixner et al. 2002; Kuji and Nakajima 2002; Emery et al. 1986).
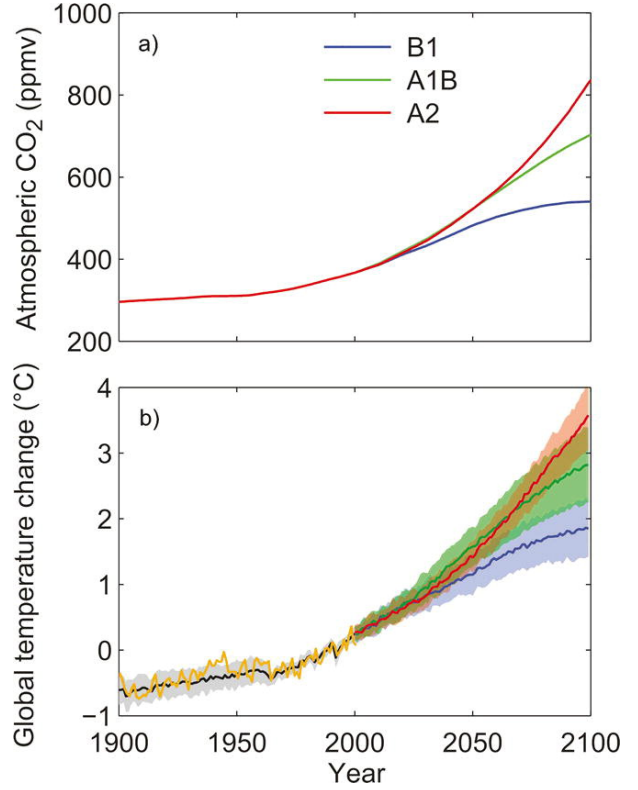
APPENDIX

Appendix Title

FIG. A1. Here is an appendix, single column figure caption.

Appendix section head

Here is a sample appendix.

$$\frac{pf\cos\phi}{p^0|\nabla h\bar{q}|(d\theta_0/dz)} \qquad (A1)$$

APPENDIX B

Second Appendix Title

a. Sample appendix section head

Second appendix example.

b. Sample appendix section head

$$\left(\frac{\partial\bar{q}}{\partial x}\overline{U'\theta'} + \frac{\partial\bar{q}}{\partial y}\overline{V'\theta'}\right) \qquad (B1)$$

References

Becker, E., and G. Schmitz, 2003: Climatological effects of orography and land–sea heating contrasts on the gravity wave–driven circulation of the mesosphere. *J. Atmos. Sci.*, **60**, 103–118, doi: 10.1175/1520-0469(2003)060⟨0103:CEOOAL⟩2.0.CO;2.

Emery, W. J., A. C. Thomas, M. J. Collins, W. R. Crawford, and D. L. Mackas, 1986: An objective method for computing advective surface velocities from sequential infrared satellite images. *J. Geophys. Res.*, **91**, 12 865–12 878, doi:10.1029/JC091iC11p12865.

Knutti, R., and Coauthors, 2008: A review of uncertainties in global temperature projections over the twenty-first century. *J. Climate*, **21**, 2651–2663, doi:10.1175/2007JCLI2119.1.

Kuji, M., and T. Nakajima, 2002: Retrieval of cloud geometrical parameters using remote sensing data. Preprints, *11th Conf. on Cloud Physics*, Ogden, UT, Amer. Meteor. Soc., JP1.7, [Available online at http://ams.confex.com/ams/pdfpapers/39550.pdf.].

Meixner, T., L. A. Bastidas, H. V. Gupta, and R. C. Bales, 2002: Multi-criteria parameter estimation for models of stream chemical composition. *Water Resour. Res.*, **38**, 1027, doi:10.1029/2000WR000112.